第 26 卷第 12 期 无 机 化 学 学 报 Vol.26 No.12
2010 年 12 月 CHINESE JOURNAL OF INORGANIC CHEMISTRY 2259-2265

钨氧化物纳米结构的合成与表征

秦玉香* 包智颖 胡 明 孙 鹏
(天津大学电子信息工程学院,天津 300072)

摘要: 采用溶剂热法以 WCl_6 作为前体合成出了一维和二维的钨氧化物纳米结构,研究了反应溶剂和前体浓度对钨氧化物物相和形貌的影响并评价了各种钨氧化物纳米结构对 NO_2 气体的敏感性能。XRD、SEM、TEM 和 XPS 的表征结果表明,通过改变溶剂和调整 WCl_6 浓度,可分别获得单斜的 $W_{18}O_{49}$ 纳米棒、$W_{18}O_{49}$ 纳米线和 WO_3 纳米片结构。气敏性能测试结果表明,钨氧化物纳米结构对 NO_2 气体表现出良好的可逆性,与 $W_{18}O_{49}$ 纳米棒和 WO_3 纳米片相比,$W_{18}O_{49}$ 纳米线对 NO_2 具有更高的灵敏度。

关键词: 氧化钨; 纳米结构; 溶剂热法; 气敏性能
中图分类号: O649 **文献标识码**: A **文章编号**: 1001-4861(2010)12-2259-07

Synthesis and Characterization of Tungsten Oxide Nanostructures

QIN Yu-Xiang* BAO Zhi-Ying HU Ming SUN Peng
(*School of Electronics and Information Engineering, Tianjin University, Tianjin* 300072)

Abstract: One- and two-dimensional tungsten oxide nanostructures were synthesized by solvothermal method using tungsten hexachloride (WCl_6) as the precursor. The effects of the solvent and the concentration of WCl_6 on the phase and the morphology of the as-synthesized tungsten oxide nanostructures were investigated and the NO_2-sensing properties were evaluated. X-ray diffraction, field emission scanning electron microscope, transmission electron microscope, X-ray photoelectron spectroscopy were employed to characterize the as-synthesized products and the results indicate that the $W_{18}O_{49}$ nanorod, $W_{18}O_{49}$ nanowire and WO_3 nanosheet with monoclinic structure can be formed by adjusting the solvent and WCl_6 concentration. The NO_2-sensing properties measurements show that the synthesized tungsten oxides have reversible response to NO_2 at different concentrations. In comparison with WO_3 nanosheet or $W_{18}O_{49}$ nanorod, the $W_{18}O_{49}$ nanowire exhibits much higher response to NO_2 gas.

Key words: tungsten oxide; nanostructure; solvothermal method; gas sensitive properties

Tungsten oxide is a versatile wide band gap semiconductor material, and it has wide applications in gas sensors[1-2], electrochromic devices[3] and photocatalysts[4]. Especially, tungsten oxide has been found to be a promising material for detection of toxic gases such as NO_x, H_2S, Cl_2, NH_3[5-6]. The gas sensing mechanism of oxide semiconductors lies in the fact that the electrical resistance of the materials will be changed when they are exposed to the gases. Consequently, the sensing response of oxides is highly dependent on their surface structure and morphology. A lot of sensing tests for tungsten oxide polycrystalline thin films indicate that the sensing response steeply increases when the grain size decreases. Recently, tungsten

收稿日期:2010-05-31。收修改稿日期:2010-08-24。
国家自然科学基金(No.60801018),天津市自然科学基金(No.09JCYBJC01100),教育部博士点新教师基金(No.200800561109)资助项目。
*通讯联系人。E-mail:qinyuxiang@tju.edu.cn
第一作者:秦玉香,女,35 岁,博士,副教授;研究方向:敏感材料与微传感器。

nanostructures such as nanowires, nanobelts and nanorods have been evaluated as ideal candidates for gas sensing applications due to their larger specific surface area and smaller dimensions compared to the Debye length[7-8]. Typically, tungsten oxide nanostructures can be fabricated by various growth techniques[9-11]. One interesting technique is solvothermal method featuring in simple operation and low cost. In this work, different tungsten oxide nanostructures including nanorod, nanowire and nanosheet were synthesized by solvothermal method. The phase and morphology of the as-synthesized tungsten oxide nanostructures were characterized and the sensing properties of the material to NO_2 gas were also evaluated.

1 Experimental

1.1 Synthesis and characterization of tungsten oxide nanostructures

Tungsten oxide nanostructures with different morphologies were synthesized by solvothermal method with tungsten hexachloride (WCl_6) as the precursor and cyclohexanol or 1-propanol as the solvent. First, a pre-determined amount of WCl_6 was dissolved in 2~4 mL ethanol to form a solution. Then, cyclohexanol or 1-propanol was added to the solution which was subsequently transferred to and sealed in a 100 mL Teflon-lined stainless steel autoclave. The concentration of WCl_6 in the solvent of cyclohexanol or 1-propanol varied from 0.003 mol·L^{-1} to 0.02 mol·L^{-1}. The solvothermal reaction was conducted at 200 ℃ for 6~9 h in an electric oven. After that, the autoclave was cooled naturally to room temperature. The final products were centrifuged and washed sequentially by deionized water and ethanol several times, and the obtained powder was dried at 70 ℃ for 6 h in air.

The crystalline phases of the tungsten oxides were analyzed using a RIGAKU D/MAX 2500V/PC X-ray diffractometer (XRD) fitted with a curved graphite diffracted-beam monochromator and 0.15 mm receiving slit and scintillation counter as the detector. The 2θ investigation region was in the range of 10°~80° with a step of 0.02° and a scanning speed of 4°·min^{-1}. Cu $K\alpha_1$ (λ=0.154 06 nm) radiation was obtained after $K\alpha_1$ stripping from a Cu X-ray target operated at 40 kV and 200 mA. The morphology and crystalline structure were observed by a FEI Nanosem 430 field emission scanning electron microscope (FESEM) at an accelerating voltage of 10 or 15 kV and a TECNAI G^{2}F-20 field emission transmission electron microscope (FETEM) operated at 300 kV of accelerated voltage. The chemical state of the tungsten oxide nanostructures was studied by X-ray photoelectron spectroscopy (XPS) using PERKIN ELEMER PHI-1600 ESCA with Mg $K\alpha$ source and a charge neutralizer. X-ray irradiation was generated under 250 W. All the binding energies were corrected for charging effect by calibration on the graphite C1*s* peak at 284.6 eV.

1.2 NO_2-sensing properties test

Gas sensors were fabricated by pouring a few drops of tungsten oxide powder-suspended ethanol onto the cleaned alumina substrates attached with a pair of interdigitated Pt electrodes with a thickness of 100 nm. The electrodes were deposited by using RF magnetron sputtering method, and the dropping suspension was prepared by ultrasonically dispersing tungsten oxide powders in ethanol for 30 min. The coated film was dried in air for 10 min. The above drop-coating process was repeated for 3 times to achieve the desired film thickness. Finally, the resulted films were heated in air using an infra-red dryer for 1 h, to evaporate the solvents residues in the coating layers.

The NO_2 gas sensing measurements were carried out in a computer-controlled gas sensing characterization system. The sensors were placed on the heating plate fixed in test chamber, and the operating temperature of the sensors was achieved by adjusting the temperature controller of the heat plate. The pure NO_2 gas was injected into the chamber directly to get the desired concentration. A professional digital multimeter with the function of measuring range automatic adjustment was used for continuously monitoring the resistance change of the sensors during the whole measurement process and the sampling interval was set to 1s. The gas response was defined as $(R_g-R_0)/R_0$, where R_g and R_0 are the resistance of a sensitive film

in a measuring gas and that in clean air, respectively.

2 Results and discussion

2.1 Effect of WCl_6 concentration on morphologies of tungsten oxide

The morphologies of tungsten oxide nanostructures synthesized at different WCl_6 concentrations in 1-propanol are shown in Fig.1(a)~(d). The solvothermal reaction temperature and reaction time were maintained constant at 200 ℃ and 9 h, respectively. It can be seen from Fig.1(a), the product synthesized at a concentration of 0.003 mol·L^{-1} exhibits ultrathin nanowire structure with diameters of several ten nanometers and lengths up to several micrometers. Further TEM investigation can identify the bundled feature, giving evidence that several nanowires with diameters of 5~10 nm assembled along their main growth direction and formed a bundled structure, as shown in the inset in Fig.1(a). This bundle structure is often formed in 1-D nanostructured materials to minimize the surface energy of the system and the lateral capillary force may act as the driving force for the nanorod assembly along the axis direction [12-13]. Increasing WCl_6 concentration to 0.01 mol·L^{-1}, it is obvious from Fig.2 (b) that the nanowire bundles become thicker, indicating that a possible agglomeration between the adjacent nanowires or nanowire bundles has occurred. The estimated bundle diameter is 40~60 nm. The inset TEM image in Fig.1(a) shows that each nanowire in the bundles is with a diameter of about 10 nm.

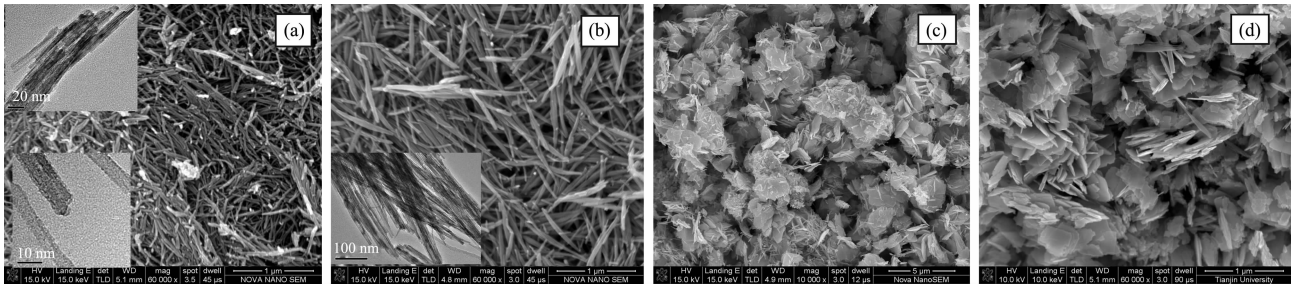

The inset in (a) and (b) is the corresponding TEM images of nanowire bundle and individual nanowire
(a) 0.003 mol·L^{-1}; (b) 0.01 mol·L^{-1}; (c) 0.015 mol·L^{-1}; (d) 0.02 mol·L^{-1}

Fig.1　SEM images of tungsten oxide nanostructures synthesize in 1-propanol at different WCl_6 concentration

When the concentration increases to 0.015 mol·L^{-1}, apparent evolution in the morphology can be observed. As shown in Fig.1(c), the product synthesized at 0.015 mol·L^{-1} is a mixture structure of nanowires and nanosheets. Up to a much higher WCl_6 concentration of 0.02 mol·L^{-1}, a pure nanosheets structure with thicknesses of 10~30 nm is obtained (Fig.1(d)). From these results, it can be speculated that the WCl_6 concentration has a great effect on the specific morphologies of tungsten oxide nanostructures synthesized by solvothermal method. This is in agreement with the previous report [14]. Low solution concentration contributes to the lower supersaturation of tungsten source, promoting the growth of tungsten oxide nanowires[15]. At higher concentration, the highly saturated WCl_6 could prohibit the growth of tungsten oxide nanowires along the main growth direction.

2.2 Effect of solvent on morphologies of tungsten oxide

Fig.2(a) and (c) respectively show the morphologies of tungsten oxide nanostructures synthesized in the solvents of 1-propanol and cyclohexanol with a constant WCl_6 concentration of 0.005 mol·L^{-1}. The solvothermal reaction in cyclohexanol and 1-propanol were conducted at 200 ℃ for 6 h and 9 h, respectively, because there was no any precipitates obtained in 1-propanol when reacting for 6 h. The SEM image shown in Fig.2(a) exhibits that the product obtained in cyclohexanol is mainly composed of short nanorods with diameter of 30~40 nm and length of 300~400 nm. Several thinner nanorods assemble together along the axis direction and form nanorod bundles. Fig.2(b) shows the TEM image of one nanorod bundle. The stacked bundles shown in Fig.2(b) can be as-

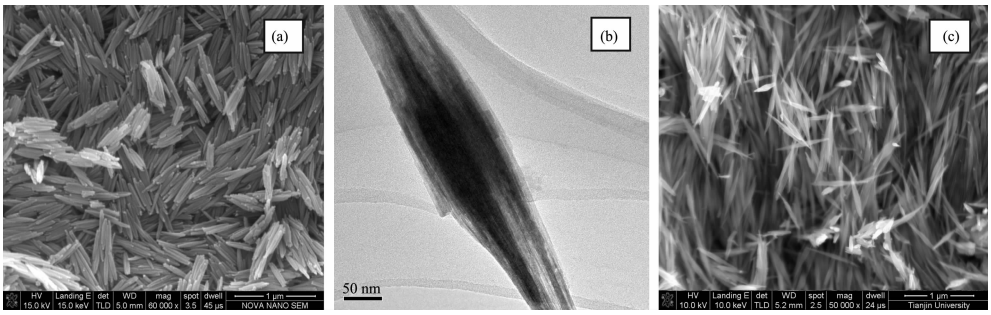

Fig.2 (a) SEM and (b) TEM images of the tungsten oxide synthesized in cyclohexanol; (c) SEM image of the tungsten oxide synthesized in 1-propanol

cribed to physical agglomeration, which can be easily dispersed by ultrasonic vibration. When substituting 1-propanol with cyclohexanol, the nanowire bundles exhibiting thin and long features are obtained, as shown in Fig.2(c).

2.3 Structure characterization of tungsten oxide nanostructures

XRD results are show in Fig.3. As shown in Fig. 3(a) and (b), the XRD patterns for the bundled tungsten oxide nanorods and nanowires synthesized by solvothermal method are very similar as evidence of the comparability of diffraction peaks in 2θ position and intensity. The main two diffraction peaks of both products can be well indexed to the monoclinic phase of $W_{18}O_{49}$ with lattice parameters of a=1.832 nm, b=0.379 nm, c=1.404 nm and β=115.04° (PDF No.65-1291). It is also observed that there are no other impurity phase peaks. The strongest peak intensity of (010) plane indicates that the growth is preferentially along the b-axis, i.e. the [010] direction. In the present experiments, the monoclinic $W_{18}O_{49}$ structures obtained in the solvent of cyclohexanol and 1-propanol are identical, which can be seen from the same diffraction peaks of monoclinic $W_{18}O_{49}$ in Fig.3. The formation of these one-dimensional nanostructures arises from the anisotropic properties of monoclinic $W_{18}O_{49}$ crystals [16]. The XRD pattern of the tungsten oxide nanosheet shown in Fig.3 (c) corresponds to the monoclinic structure of WO_3 with lattice of a=0.729 7 nm, b=0.753 9 nm, c=0.768 8 nm and β=90.91° (PDF No. 43-1035). From this XRD pattern, the two strongest diffraction peaks appear at 2θ=23.58° and 2θ=24.34° corresponding to (020) and (200) facets and the peak intensity of the (002) reflection is much weaker, which implies that the nanosheets grow along the [010] and [100] crystallographic direction and are enclosed by ±(001) facets.

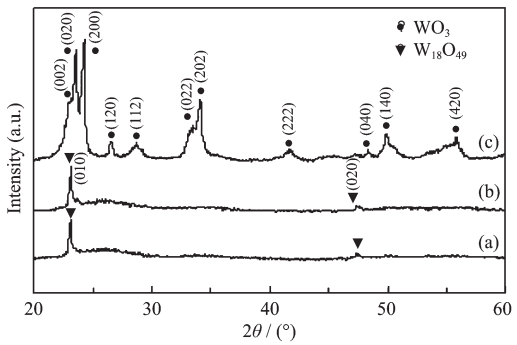

(a) nanorods; (b) nanowires; (c) nanosheets

Fig.3 XRD patterns of the as-synthesized tungsten oxide nanostructures

Fig.4 (a)~(c) show the high resolution (HR) TEM images of the nanorod, nanowire and nanosheet. Here, the lattice spacings for nanorod and nanowire are 0.378 nm and 0.380 nm, respectively, corresponding to (010) plane of monoclinic $W_{18}O_{49}$ according to PDF No.65-1291. This result indicates that the as-synthesized one-dimensional nanostructures all consist of monoclinic $W_{18}O_{49}$ and the dominant growth direction is along the b-axis direction. The HRTEM of tungsten oxide nanosheet indicates that the crystal plane distances are about 0.363 nm and 0.378 nm, almost equal to the crystal plane distance of monoclinic WO_3 (200) and (020) planes, respectively. The results shown in Fig.4 are in agreement with the ones from XRD characterization (Fig.3).

XPS spectra are shown in Fig.5, which highlights the survey and the high-resolution spectra of W4*f*

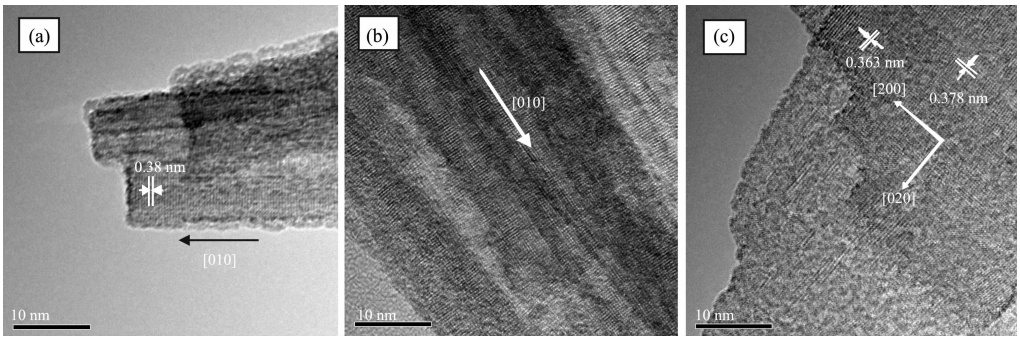

Fig.4　HR-TEM images of as-synthesized (a) nanowire, (b) nanorod and (c) nanosheet

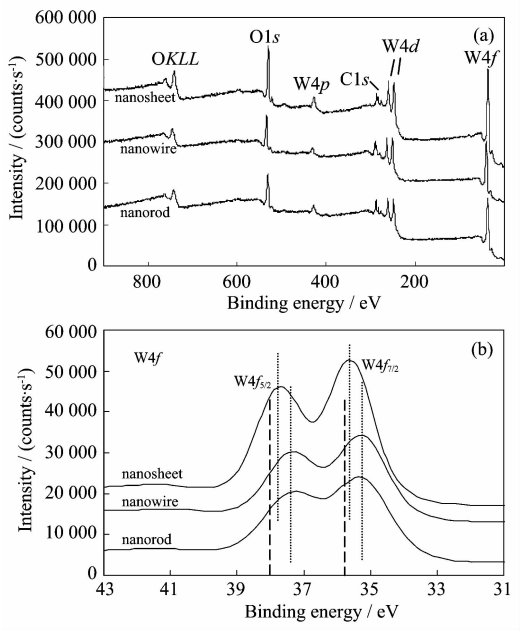

(a) the survey XPS spectra; (b) W4*f* high-resolution spectra

Fig.5　XPS spectra of tungsten oxide nanorod, nanowire and nanosheet

peaks. Tungsten is identified in the survey spectrum (Fig.5(a)) by the presence of the W4*f*, W4*d*, and W4*p* transitions. Also labeled are the O*KLL* and O1*s* features and the C1*s* line probably coming from the surface contamination during the annealing treatment. Fig.5(b) shows the high-resolution spectra of the W4*f* region, which contains the W4$f_{7/2}$ and W4$f_{5/2}$ peaks with binding energies of 35.2/35.2/35.7 eV and 37.2/37.2/37.8 eV for nanorod/nanowire/nanosheet, respectively. It is well established that the fully oxidized tungsten oxide (WO_3) has the doublet due to W4$f_{7/2}$ at 35.8 eV and W4$f_{5/2}$ at 38 eV, which represents the W^{6+}[17]. In Fig.5(b), the position shift of the peaks corresponding to W4$f_{7/2}$ and W4$f_{5/2}$ indicates that there are some oxygen vacancies existing in three tungsten oxide nanostructures. The larger peaks shift of tungsten oxide nanorod and nanowire implies much more oxygen vacancies. Because the electron density in semiconductors depends on the density of oxygen vacancies, the vacancies play a significant role in the gas detection mechanism for the oxide semiconductors[18], and the existence of oxygen vacancies is much beneficial to the gas-sensing application of this kind of materials. From Fig.5(b), it also can be seen that, for the nanorods and nanowires, the binding energies for the peaks of W4$f_{7/2}$ and W4$f_{5/2}$ are the same, which suggests the same W valence state. This result is consistent with the one of XRD measurements that the nanorod and nanowire has the same crystalline structure of monoclinic $W_{18}O_{49}$.

2.4　Gas sensing properties

The gas-sensing properties of the as-synthesized tungsten oxide nanostructures were evaluated upon exposure to NO_2 gas. Fig.6 shows the dynamic responses of tungsten oxide nanorod, nanowire and nanosheet to NO_2 gas at an operating temperature of 200 ℃. As shown in the figure, the measured resistances increase upon exposure to NO_2 gas. This result is expected because the oxidizing analyte NO_2 withdraws electrons from the *n*-type tungsten oxide surface and induces the formation of electron-depleted space-charge layers[19]. Notably, the resistances could almost recover to its initial value after NO_2 removal, indicating a good reversibility of these nanostructure materials. Fig.7 shows the effect of NO_2 concentration in the range of 1 ~ 20 $\mu L \cdot L^{-1}$ on the responses of tungsten oxide nanostructures at 200 ℃. From the figure, the $W_{18}O_{49}$

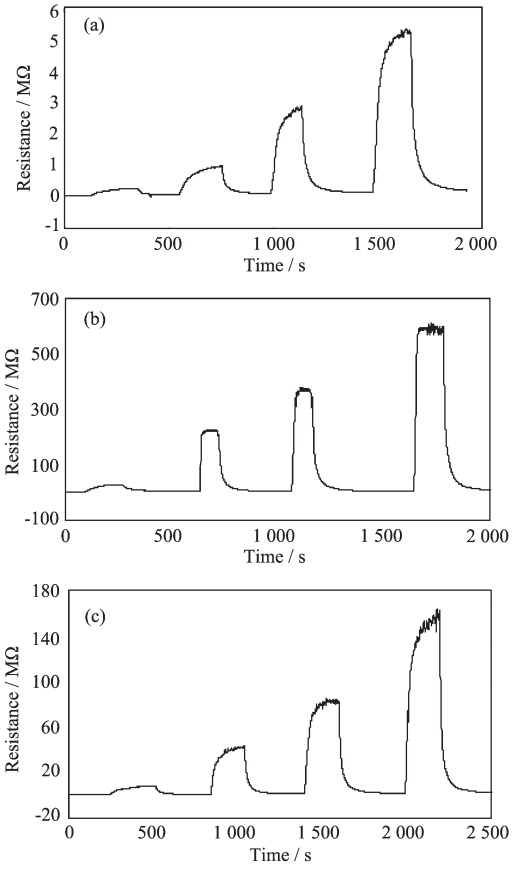

(a) nanorod; (b) nanowire; (c) nanosheet

Fig.6 Dynamic response of tungsten oxide nanostructure to varying NO_2 concentration at an operating temperature of 200 ℃

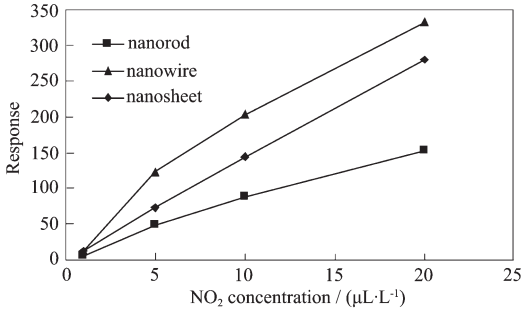

Fig.7 NO_2 gas response of tungsten oxide nanostructures as a function of NO_2 concentration at an operating temperature of 200 ℃

nanowire shows the highest response at different NO_2 concentrations, while the lowest response is obtained from the $W_{18}O_{49}$ nanorod. The response values of the $W_{18}O_{49}$ nanowires upon exposure to 1, 5, 10 and 20 $\mu L \cdot L^{-1}$ NO_2 are 13.4, 123.6, 203.4 and 332.3, while those of the WO_3 nanorod are 6.9, 49.7, 89.1 and 152.8, respectively.

Tungsten oxide is a typical n-type semiconductor, and its gas-sensing mechanism belongs to the surface-controlled type, i.e. the change in resistance of tungsten oxide is primarily caused by the adsorption and desorption of the gas molecules on the surface of the sensing film[20-21]. Atmospheric oxygen absorbed on the oxide surface captures electrons from the conduction band of tungsten oxide and forms chemisorbed O^-, O^{2-} and O_2^-, creating a thin electron-depleted space-charge layer at the surface of the oxide. When the tungsten oxide is exposed to the oxidizing NO_2, the gas molecules can be directly adsorbed onto the surface by extracting electrons from the conduction band (Eq.(**1**) and (**2**)) or they can interact with the chemisorbed oxygen on the surface (Eq.(**3**) and (**4**))[22-23]:

$$NO_2(gas)+e^- \rightleftharpoons NO_2^-(ads) \quad (\mathbf{1})$$

$$NO_2(gas)+e^- \rightleftharpoons NO(gas)+O^-(ads) \quad (\mathbf{2})$$

$$NO_2(gas)+O_2^-(ads)+2e^- \rightleftharpoons NO_2^-(ads)+2O^-(ads) \quad (\mathbf{3})$$

$$NO_2(gas)+O^-(ads) \rightleftharpoons NO^+(ads)+2O^-(ads) \quad (\mathbf{4})$$

These reactions consume further electrons in the conduction band of tungsten oxide, leading to an increase of the electron-depleted layer and the height of the Schottky barrier, which then leads to the increase in the resistance. Therefore, large specific surface area is beneficial to achieving a high gas response. In our experiments, Brunauer-Emmett-Teller (BET) gas-sorption measurements were employed to evaluate the specific surface area of the as-synthesized tungsten oxide nanostructures by using Quantachrome NOVA automated gas sorption system. The measurements results show that the $W_{18}O_{49}$ nanowires have much larger specific surface area (90 $m^2 \cdot g^{-1}$) than the WO_3 nanosheets (47 $m^2 \cdot g^{-1}$) or $W_{18}O_{49}$ nanorods (69 $m^2 \cdot g^{-1}$). The larger surface area can provide more adsorption-desorption sites and a larger amount of surface adsorbed oxygen species interacting with detected gas molecules. Thus, $W_{18}O_{49}$ nanowires with higher specific surface area can show much larger change in resistance upon exposure to NO_2 than the WO_3 nanosheets or $W_{18}O_{49}$ nanorod with lower specific surface area. Another important factor for high response of $W_{18}O_{49}$

nanowire is its non-stoichiometric crystal structure[24]. There exist much more oxygen vacancies in the crystal structure of non-stoichiometric $W_{18}O_{49}$ than fully oxidized WO_3[17], as indicated from the XPS results in Fig. 5. The large amounts of oxygen vacancies can serve as adsorption sites of gas molecular and effect on the electron density in oxide, which is beneficial to achieving much higher gas response[18,25]. Above analysis can explain why the $W_{18}O_{49}$ nanowires exhibit higher response than the WO_3 nanosheets or $W_{18}O_{49}$ nanorod. However, as shown in Fig.7, the non-stoichiometric $W_{18}O_{49}$ nanorod with higher specific surface area shows lower NO_2 response than the stoichiometric WO_3 nanosheet with lower specific surface area. This result can be explained from their different microstructure. Comparing the SEM images of WO_3 nanosheet and $W_{18}O_{49}$ nanorod (Fig.1(d) and Fig.2(a)), it is clear that, differing from the compact structure of nanorod, the nanosheets support each other and form a loose and porous structure which is convenient for the diffusion of NO_2 gas in the bulk of nanosheets film. It is possible that the loose and porous structure dominate the high response of WO_3 nanosheet.

3 Conclusion

Tungsten oxide nanostructures including nanowire, nanorod and nanosheet were synthesized by solvothermal method with tungsten hexachloride (WCl_6) as the precursor. One-dimensional $W_{18}O_{49}$ nanowire bundles are obtained in 1-propanol at WCl_6 concentration below 0.01 mol·L^{-1}, while the structure of pure two-dimensional WO_3 nanosheet was formed at concentration of 0.02 mol·L^{-1}. In the solvent of cyclohexanol, $W_{18}O_{49}$ nanorod is formed at WCl_6 concentration of 0.005 mol·L^{-1}. The as-synthesized tungsten oxide nanostructure exhibits reversible response to NO_2 at different concentrations. In comparison with WO_3 nanosheet or $W_{18}O_{49}$ nanorod, the $W_{18}O_{49}$ nanowire exhibits much higher response to NO_2 gas due to its much larger specific surface area and non-stoichiometric crystal structure.

References:

[1] Li X L, Lou T J, Sun X M, et al. *Inorg. Chem.*, **2004**,**43**:5442-5449

[2] Ponzoni A, Comini E, Sberveglieri G, et al. *Appl. Phys. Lett.*, **2006**,**88**:203101

[3] Santato C, Odziemkowski M, Ulmann M. *J. Am. Chem. Soc.*, **2001**,**123**:10639-10649

[4] DU Jun-Ping(杜俊平), CHEN Qi-Yuan(陈启元), ZHAO Juan(赵　娟), et al. *Chinese J. Inorg. Chem.*(*Wuji Huaxue Xuebao*), **2007**,**23**:1005-1010

[5] LI Ling(李　玲), PAN Qing-Yi(潘庆谊), CHENG Zhi-Xuan(程知萱), et al. *J. Inorg. Mater.*, **2006**,**21**:151-156

[6] Choi Y G, Sakai G, Shimanoe K, et al. *Sens. Actuators B*, **2004**,**101**:107-111

[7] Pan Z W, Dai Z R, Wang Z L. *Science*, **2001**,**291**:1947-1949

[8] Cui Y, Lieber C M. *Science*, **2001**,**291**:851-853

[9] Sun S B, Zou Z D, Min G H. *Mater. Charact.*, **2009**,**60**:437-440

[10]Ha J H, Muralidharan P, Kim D K. *J. Alloy. Compd.*, **2009**, **475**:446-451

[11]Huang K, Pan Q T, Yang F, et al. *Appl. Surf. Sci.*, **2007**, **253**:8923-8927

[12]Pfeifer J, Badaljan E, Tekulabuxbaum P, et al. *J. Cryst. Growth*, **1996**,**169**:727-733

[13]Kwan S, Kim F, Akana J, et al. *Chem. Commun.*, **2001**,**5**: 447-448

[14]Moon J, Carasso M L, Krarup H G, et al. *J. Mater. Res.*, **1999**,**14**:866-875

[15]Choi H G, Jung Y H, Kim D K. *J. Am. Ceram. Soc.*, **2005**, **88**:1684-1686

[16]Xia Y N, Yang P D, Sun Y G, et al. *Adv. Mater.*, **2003**,**15**: 353-389

[17]Liao C C, Chen F R, Kai J J. *Sol. Energy Mater. Sol. Cells*, **2007**,**91**:1258-1266

[18]Gopel W, Schierbaum K D. *Sens. Actuators B*, **1995**,26-27: 1-12

[19]Park C O, Akbar S A. *J. Mater. Sci.*, **2003**,**38**:4611-4637

[20]Mizsei J. *Sens. Actuators B*, **1993**,**23**:173-176

[21]Rothschild A, Komem Y. *J. Appl. Phys.*, **2004**,**9**:6374-6380

[22]Safonova O V, Delabouglise G, Chenevier B, et al. *Mater. Sci. Eng. C*, **2002**,**21**:105-111

[23]Sayago I, Gutirrez J, Ars L, et al. *Sens. Actuators B*, **1995**, **25**:512-515

[24]Zhao Y M, Zhu Y Q. *Sens. Actuators B*, **2009**,**137**:27-31

[25]Jiménez I, Centeno M A, Scotti R, et al. *J. Electrochem. Soc.*, **2003**,**150**:72-80